JPhys Energy

PAPER • OPEN ACCESS

Defects modification in thermoelectric Mg_2Sn (Ge) epitaxial thin films through modulation of Mg flux rate in MBE

To cite this article: Kenneth Magallon Senados *et al* 2025 *J. Phys. Energy* **7** 035001

Journal of Physics: Energy

PAPER

Defects modification in thermoelectric Mg_2Sn (Ge) epitaxial thin films through modulation of Mg flux rate in MBE

Kenneth Magallon Senados[1,2,*], **Takashi Aizawa**[2], **Isao Ohkubo**[2], **Takahiro Baba**[2], **Akira Uedono**[1], **Takeaki Sakurai**[1,*] and **Takao Mori**[1,2]

[1] Graduate School of Pure and Applied Sciences, University of Tsukuba, 1-1-1 Tennodai, Tsukuba, Ibaraki 305-8573, Japan
[2] Research Center for Materials Nanoarchitectonics (MANA), National Institute for Materials Science (NIMS), 1-1 Namiki, Tsukuba, Ibaraki 305-0044, Japan
[*] Authors to whom any correspondence should be addressed.

E-mail: senados.kenneth.magallon.tkb_gm@u.tsukuba.ac.jp and sakurai.takeaki.ft@u.tsukuba.ac.jp

Keywords: thin film thermoelectric, Mg_2Sn (Ge), epitaxial growth, defects

Supplementary material for this article is available online

OPEN ACCESS

RECEIVED
9 September 2024

REVISED
5 February 2025

ACCEPTED FOR PUBLICATION
23 March 2025

PUBLISHED
2 April 2025

Abstract

Precise defect control is crucial for optimizing thermoelectric (TE) materials. However, thin film processes differ from bulk synthesis, necessitating distinct approaches to defect management. This study investigates the impact of varying Mg flux rates in the molecular beam epitaxy (MBE) growth of epitaxial Mg_2Sn (Ge) thin films, with Mg: Sn (Ge) ratios from 3.9 to 9.1 while maintaining constant Sn and Ge flux rates. Our results indicate that while the films mainly consisted of the Mg_2Sn phase due to excess Mg compensating evaporation at the growth temperature, the Mg flux rate significantly influenced film growth dynamics. X-ray diffraction analysis showed that higher Mg flux rates increased microstrain and decreased vertical grain sizes, suggesting increased planar defect density. However, the full-width half maximums of rocking curves tend to be reduced at higher flux rates, attributed to enhanced in-plane grain alignment and reduction of point defect density. Positron annihilation experiments revealed lower vacancy-type defects at higher Mg flux rates, aligning with the rocking curve measurements. The higher Mg flux rates enhanced surface migration and promoted larger horizontal grain growth. As these grains coalesce, slight misalignments between them introduce strain within the crystal lattice. To accommodate this strain, planar defects such as stacking faults form, as indicated by the x-ray pole figure measurements. Despite the higher crystal quality and reduction in vacancy-type defects, the total thermal conductivity of the films decreased with increasing Mg flux rates. This suggests that modulating Mg flux rates in MBE-grown Mg_2Sn thin films, it is possible to achieve enhanced crystalline alignment and controlled formation of beneficial higher-dimensionality defects, which together contribute to the reduction in thermal conductivity and improve the film's overall TE performance.

1. Introduction

Defects in thermoelectric (TE) materials are pivotal in shaping their performance, influencing electrical and thermal conductivity, ultimately dictating TE efficiency [1–6]. The quest for optimal TE performance confronts significant challenges, notably the intricate interplay between material defects and structural dimensions [7–9]. As a promising foundation of miniaturized TE devices, thin films offer scalability, flexibility, and seamless integration with device architectures, rendering them highly attractive for self-powered Internet of Things (IoT) applications [10–13]. However, the unique growth dynamics and surface interactions inherent in thin film deposition techniques introduce novel challenges in balancing crystal quality and defect management. Controlling defects in thin films demands a more nuanced approach compared to bulk synthesis methods, owing to factors such as surface migration, epitaxial growth, and interfacial interactions [14–18]. Advanced TE device designs, such as segmented TE modules, further

highlight the importance of optimizing material properties for specific operating conditions to achieve maximum efficiency and performance [19]. A comprehensive understanding of how defect formation and manipulation differ in thin film materials is crucial for improving thin-film-based TE device performances.

In thin film fabrication, the precise manipulation of defect densities and distributions may be achievable through tailored deposition techniques, growth conditions, and/or post-processing treatments [20–23]. While conventional methods like physical vapor deposition, chemical vapor deposition, and sputtering provide general applicability, their precision often falls short for certain applications. Notably, molecular beam epitaxy (MBE) presents a promising avenue for defect control [24, 25]. Operating under ultra-high vacuum conditions, MBE facilitates the growth of epitaxial layers with high control over crystal structure and atomic arrangement. This method allows for depositing materials atom by atom or molecule by molecule, ensuring remarkably low defect densities and well-defined interfaces. Consequently, the MBE technique may also offer the potential to engineer defects in TE thin films, thereby fine-tuning electron and phonon transport properties to improve the TE performance of our thin films.

MBE has been successfully employed to produce high-quality Mg_2Sn epitaxial thin films, and its applicability to miniaturized TE devices has also been demonstrated [26–30]. This underscores the potential of Mg_2Sn-based thin films and their derivatives as promising candidates for low-cost, low-toxicity materials in IoT applications, particularly within moderate temperature ranges. In our prior investigations, we have analyzed the surface chemical states, structures, and defect formations in epitaxial $Mg_2Sn_{1-x}Ge_x$ thin films which are deemed necessary for successful integration in microscale TE devices [31, 32]. Specifically, one of our findings indicates that several factors, such as the incorporation of Ge, can influence defect formations in these films. We observed a decrease in the concentration of vacancy-type point defects with increasing Ge concentration. This suggests that by examining different growth process variables, including Ge concentration, we can potentially control the defects in MBE-grown films.

In the growth of high-quality films via MBE, numerous other variables can be independently controlled, with the flux rate being a key parameter adjusted by manipulating the evaporation rate of the source materials [33]. Since MBE growth occurs under nonequilibrium conditions, the flux rates of source materials significantly influence the resulting film properties. For instance, in the epitaxial film formation of Mg_2Sn, varying the Sn flux rate while fixing the Mg flux rate can yield different outcomes. It has been observed that a low Sn flux rate below 2 atoms·s^{-1}·nm^{-2} is essential for achieving high-quality crystalline epitaxial films. Conversely, higher Sn flux rates have been associated with the formation of secondary orientations of Mg_2Sn and β-Sn phases [26].

In this study, we closely examine how modulation of Mg flux rates in MBE growth of Mg_2Sn (Ge) impacts the crystal quality and formation of defects in these epitaxial films. Although excess Mg, which has a high vapor pressure, would predominantly desorb during film growth, the modulation of Mg flux rates plays a significant role in influencing both film quality and the concentration of point defects.

2. Experimental methods

Mg_2Sn (Ge) epitaxial thin films were grown using an MBE system (Eiko, EV-500) under vacuum conditions of 10^{-6}–10^{-7} Pa on sapphire (0001) substrates. The substrates were cleaned ultrasonically in acetone and subsequently heated at 1000 °C for 1 h in the MBE chamber before growth. Mg_2Sn (Ge) films were grown with varying Mg flux rates from 6.0–18.0 atoms·s^{-1}·nm^{-2}, while maintaining the Sn (Ge) flux rate constant 1.65 atoms·s^{-1}·nm^{-2}. The Ge fraction was kept at 5% with respect to Sn. Elemental magnesium (>99.95%), tin (>99.999%), and germanium (>99.999%) metals were evaporated using conventional effusion cells with pyrolytic boron nitride crucibles at 370°C–410 °C for Mg, 1100°C–1120 °C for Sn, and 1050°C–1150 °C for Ge. The substrate temperatures and the deposition times were fixed at 380 °C and 30 min, respectively. The crystal quality was evaluated by x-ray diffraction (XRD) patterns of θ–2θ scans, rocking curves, and pole figures measured by Rigaku SmartLab x-ray diffractometer. Nano-scale structural evaluation of the cross-section of the films was performed using a transmission electron microscope (TEM; Talos F200X G (2) (S)TEM, Thermo Scientific) at 200 kV acceleration voltage with a magnification accuracy of ±10%. The hall coefficient (R_H) was measured using Van der Pauw's method in DC mode at room temperature (RT), with a 0.32 T magnetic field using a Bio-RAD-H5580 hall measurement machine with an R_H measurement uncertainty of approximately 10%. The carrier concentration (p) and mobility (μ) were calculated by $p = 1{\cdot}[e{\cdot}R_H]^{-1}$ and $\mu = R_H{\cdot}[\rho]^{-1}$, where e and ρ are elementary charge and resistivity, respectively. Electrical conductivities, Seebeck coefficient, and power factors were measured by the four-probe method at RT using a ZEM 3 (ULVAC Advance Riko) apparatus under a He atmosphere. The thermal conductivities were measured along the cross-plane by a pico-second time-domain thermoreflectance apparatus in a front-heating/front-detection configuration (Netzsch-Geratebau GmbH) whose measurement details are described elsewhere [34–37]. The thermal conductivity was obtained by $\kappa = \lambda \cdot d \cdot C_p$, where λ is the thermal

diffusion, d is density, and C_p is heat capacity in constant pressure of Mg_2Sn [38]. Vacancy-type defects in the films were probed using positron annihilation spectroscopy (PAS). Details regarding the measurements involving PAS and additional information on the measurement are described elsewhere [39–42].

3. Experimental results

Mg_2Sn (Ge) film growth was carried out under the Mg flux rate range between 8.5 and 15 atoms·s^{-1}·nm^{-2}. Our preliminary investigation revealed that films grown at flux rates below 8.5 atoms·s^{-1}·nm^{-2} resulted in poor film quality, probably due to secondary Sn phases as observed in the cross-section TEM image in figure S1(a). Conversely, films grown at the flux rates above 15 atoms·s^{-1}·nm^{-2} also resulted in poor film quality, with clear separation between Mg_2Sn and Mg phases, as shown in figure S1(b).

Figure 1(a) shows the XRD patterns of Mg_2Sn (Ge) films grown with varying Mg flux rates. All samples exhibited strong Mg_2Sn (nnn) peaks ($n = 1$–4), indicating that despite the variations in the flux rate ratio of Mg: Sn (Ge) by varying the Mg flux rate, and even though the relative Mg supply rate largely exceeded to reach 2 in the Mg/Sn (Ge) ratio, the resulting films consisted of the Mg_2Sn phase as the main component. This occurrence is attributed to the excess Mg easily evaporating at the growth temperature of 380 °C. Figure 1(b) illustrates the changes in the Mg_2Sn (111) peak, where an increase in intensity and a slight shift to a lower diffraction angle are observed with increasing Mg flux rate. While the enhanced intensity of the (111) peak might suggest improved structural aspects of the Mg_2Sn (Ge) films, it was however observed that the full-width half maximum (FWHM) broadened suggesting the presence of increasing strain or compositional inhomogeneity at higher Mg flux rates which could introduce defects or phases with slightly different lattice structures. Notably, when considering the XRD Mg_2Sn (111) peak intensities normalized by both film thickness d (detailed in supplementary table S1) and substrate peak intensity $I_{saaphire(00012)}$, i.e. $I_{norm} = I_{Mg_2Sn(111)}/(I_{sapphire(00012)}d)$ [43], the normalized intensity, as shown in the inset of figure 1(b), reveals that the increase in peak intensity is primarily due to structural changes rather than variations in film thickness. Complementary to this, the rocking curve measurements shown in figure 1(c) reveal a decrease in FWHM at higher flux rates, indicating improved in-plane grain alignment. This suggests that while the films experience strain or inhomogeneity in the vertical direction, the overall in-plane crystalline alignment is enhanced with increasing Mg flux. In addition to the Mg_2Sn (111) and the substrate peaks, a small diffraction peak appears at 34° in the high Mg flux rate (∼15 atoms·s^{-1}·nm^{-2}) samples (figure 1(a)), which can be assigned as Mg (111) diffraction. The peak shift of Mg_2Sn (111) toward the lower diffraction angle indicates the expansion of Mg_2Sn lattice.

The microstructural parameters, including d-spacing and the FWHM of the rocking curve, were derived from the Mg_2Sn (111) peak in the θ–2θ XRD data, as depicted in figure 1(d). The analysis reveals a slight increase in the d-spacing at higher flux rates, confirming lattice expansion. Higher Mg flux rates introduce more Mg atoms into the lattice, causing expansion and a modest increase in the FWHM of the Mg_2Sn(111) peak in the θ–2θ XRD data from 0.173° to 0.185°. This suggests a potential increase in strain or compositional inhomogeneity due to localized lattice distortions at higher flux rates.

The decrease in the FWHM of the rocking curve at higher flux rates suggests improved in-plane grain alignment due to enhanced surface diffusion and better lateral growth. However, the modest increase in the FWHM of the θ–2θ scan at higher flux rates points to increased lattice strain or compositional inhomogeneity. The introduction of Mg atoms at higher rates may lead to structural adjustments within the lattice, contributing to the observed broadening.

To elucidate the presence of defects, cross-sectional TEM observations of the grown films were conducted. Figures 2(a)–(c) illustrates the representative TEM images of the films. Parallel Moiré patterns are seen in all the films grown. Moiré patterns are known to arise when two periodic structures with slightly different lattice periodicities or orientations are superimposed, creating an interference pattern that appears as regular stripes or grids in high-resolution images.

In our study, these patterns may be influenced by structural variations within Mg_2Sn, potentially including regions with differing Mg vacancy (V_{Mg}) concentrations, as suggested by previous studies [44–46]. Introducing V_{Mg} into Mg_2Sn slightly reduces the lattice constant, as the absence of Mg atoms affects local bonding and atomic spacing. This could create nanoscale regions with slightly different lattice periodicities. If such regions form semi-coherent interfaces, interference between their periodic lattice modulations may contribute to the observed Moiré patterns. However, other structural factors, such low-angle grain boundaries, may also be involved.

The fast Fourier transform (FFT) of the regions enclosed in yellow lines, shown as an inset in the TEM image, reveals a diffraction pattern characteristic of a single-crystal region, with additional spots around the fundamental diffraction spots attributed to contributions from the parallel Moiré patterns. Figure 2(a) shows a relatively uniform structure with less pronounced stress and fewer defects. As the Mg flux rate increases in

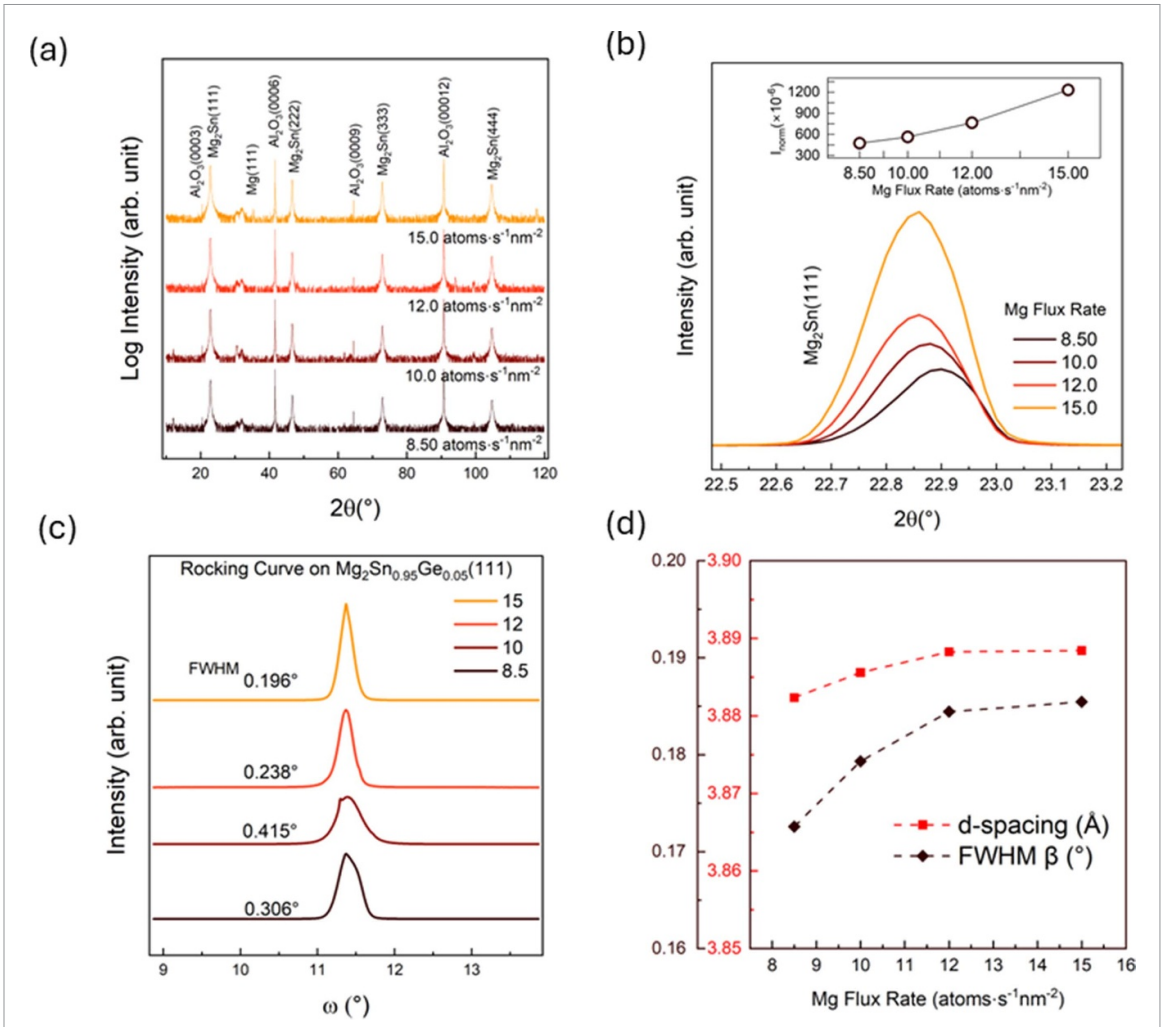

Figure 1. (a) XRD patterns of Mg_2Sn (Ge) thin films with varying Mg flux rates. (b) The peaks change on Mg_2Sn (111), (c) x-ray rocking curve at (111) and (d) microstructural analysis of XRD (111) peak.

figure 2(b), more defects and strain contrast are visible, indicating increased lattice distortions. In figure 2(c), at the highest Mg flux rate, Moiré patterns are still observable; however, additional features which appear to be more complex than the surrounding areas are also visible. The diffraction pattern of this region exhibits extra spots, suggesting the presence of longer-range ordering in the crystal lattice. The longer-range ordering, observed in the TEM image, appears to extend over a region approximately 15–25 nm in size, which could be due to the formation of a metastable modulated structure. This structural modulation might also contribute to the broadening of the (111) peak observed in the XRD pattern, as it introduces additional strain or defects into the lattice. The formation of this state could be a result on non-equilibrium conditions during the high Mg flux deposition but while this feature may indicate a metastable state, further analysis is needed to confirm the exact nature of these structures.

To further analyze the structural distortions, we performed an Inverse FFT (IFFT) analysis on one Moiré pattern region enclosed in red in figure 2(b), with results shown in figure 2(e). IFFT was performed to enhance the visualization of lattice distortion and dislocations at the interfaces, which may contribute to the observed Moiré patterns. The IFFT reveals the presence of dislocations in the Moiré patterns. These dislocations, consistent with semi-coherent interface models [45], contribute to the periodic lattice modulations responsible for the observed Moiré patterns.

While our findings suggest that vacancy-induced structural variations may contribute to the formation of Moiré patterns, other mechanisms, such as low-angle grain boundaries characterized by slight misorientations between adjacent grains, may also play a role. However, our current data does not provide conclusive evidence to distinguish between these mechanisms, and further investigation is needed.

To investigate the changes in the concentration of vacancy-type defects in the films, we performed PAS measurements using a monoenergetic positron beam. Figure 3 shows the sharpness (S) parameter of the Mg_2Sn (Ge) films as a function of incident positron energy (E). The S-parameter is used to analyze the defect

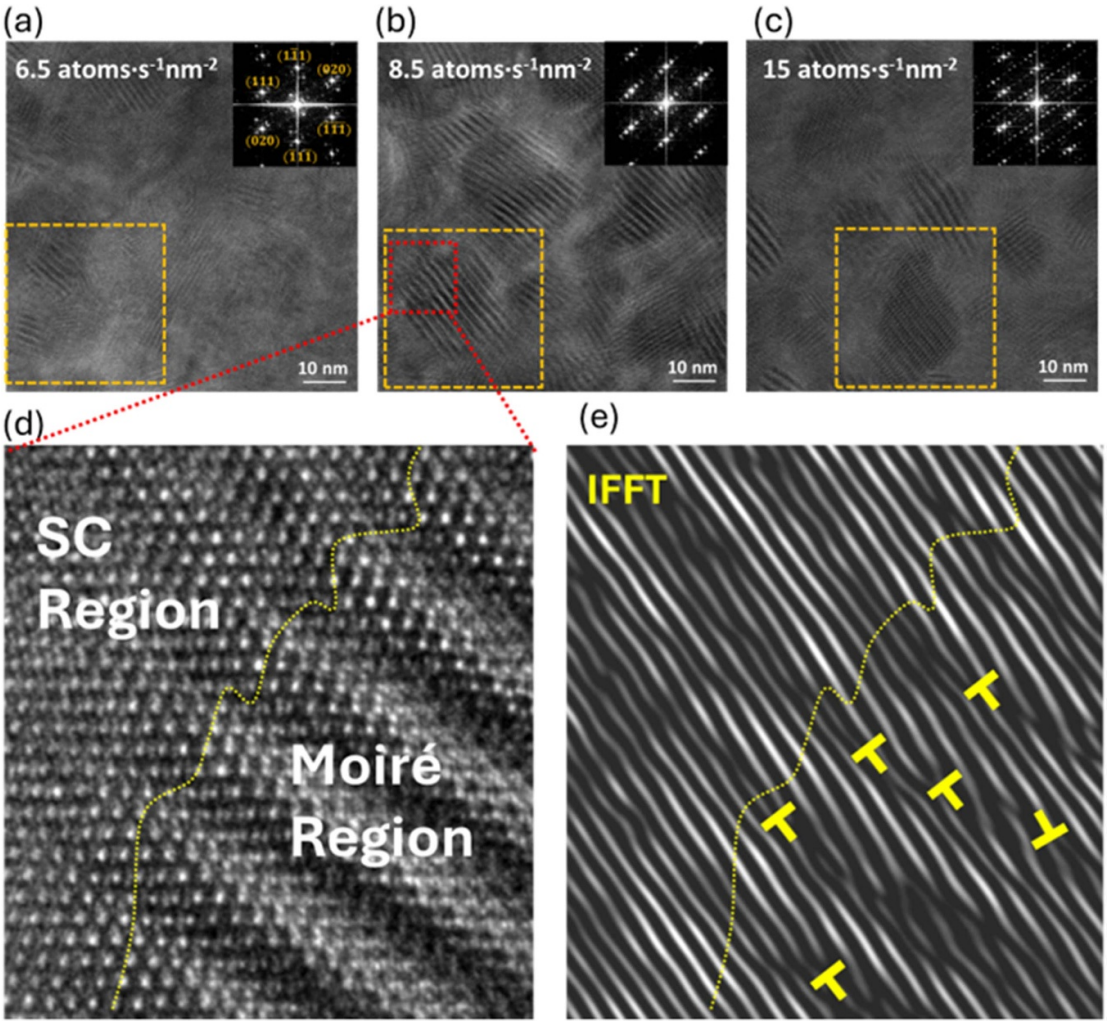

Figure 2. (a)–(c) Cross-sectional high-magnification TEM images of $Mg_2Sn_{0.95}Ge_{0.05}$ thin films grown at three different Mg flux rates, with FFT patterns of the regions enclosed by yellow squares shown as insets. (d) Higher magnification of the region outlined in red in (b). (e) IFFT image of the region in (d), highlighting dislocations.

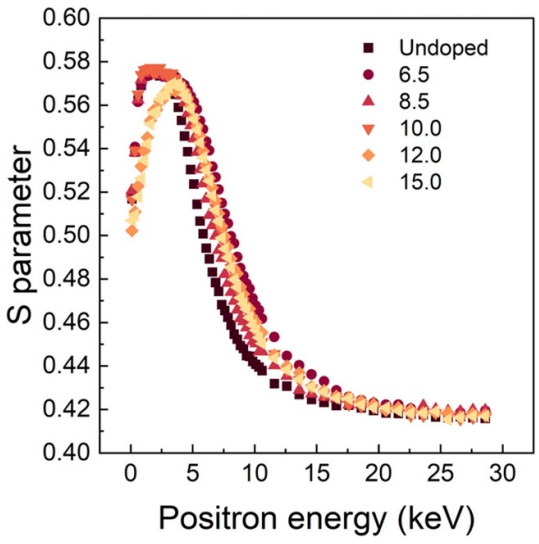

Figure 3. S parameter as a function of the incident photon energy E of the thin films.

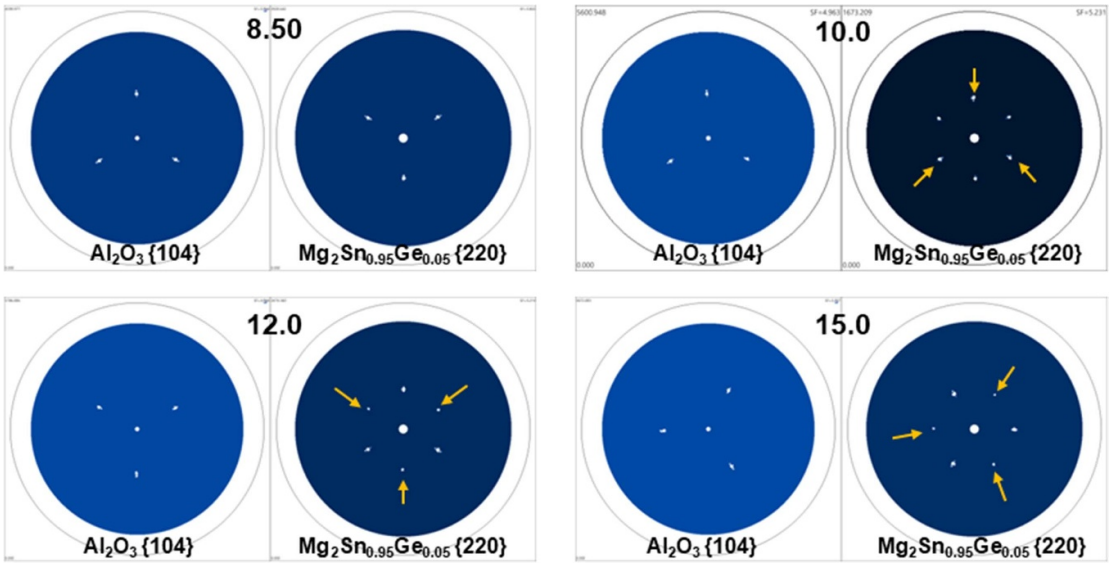

Figure 4. X-ray pole figures of Al_2O_3 {104} and Mg_2Sn (Ge) {220} thin films with varying Mg flux rate.

concentration or defect-related characteristics in a material. The results indicated that there was a depth distribution of vacancy-type defects in the films, which are V_{Mg} as we previously suggested [32]. For positron energies below approximately 4 keV, positrons predominantly annihilate within the films, while at higher energies they penetrate deeper, eventually annihilating near the substrate, where the S parameter approaches a value of approximately 0.42.

The energy position of the transition from film to substrate annihilation (e.g. where S(E) $\approx$ 0.48) depends on the film thickness, which is detailed in supplementary table S1. Thicker films require higher positron energies for positrons to penetrate to the substrate, resulting in a delayed transition, whereas thinner films exhibit this transition at lower energies. For example, the undoped Mg_2Sn sample, exhibited the lowest thickness, leading to an earlier transition to the substrate compared to the thicker Ge-alloyed films. While a simple proportionality might be expected, the observed variation in energy (6.5–9 keV) is larger than the 13% thickness increase (186–210 nm). This deviation may arise due to several factors such as variations in film density, interface roughness, or other factors affecting positron penetration depth. While the general trend between film thickness and required positron energy follows expectations, the observed deviation suggests that additional factors, such as interface effects or density variations, may influence positron penetration. Further investigation would be needed to model this relationship more precisely.

At very low positron energies ($E < 0.5$ keV), positrons may annihilate from bound surface states, typically corresponding to an S parameter of approximately 0.50. This surface-state annihilation is observed in all samples but is more pronounced in films grown at lower Mg flux rates. At low Mg flux rates, the S parameter transitions to the bulk annihilation value ($\approx$0.58) more quickly. This is due to shorter positron diffusion lengths, consistent with higher concentrations of vacancy-type defects. Vacancies act as positron traps, reducing the distance positrons can travel before annihilation. For positron energies in the range $E = 0.5$–4 keV, corresponding to annihilation within the films, no significant change in the S values was observed for samples grown with Mg flux rates of 6.5–10.0 atoms·s^{-1}·nm^{-2}. However, for samples grown at flux rates of 12.0–15.0 atoms·s^{-1}·nm^{-2}, the S values at $E < 3$ keV decreased.

This reduction in S values at higher Mg flux rates can be attributed to two factors. First, excess Mg atoms at high flux rates may diffuse into the lattice, interact with existing vacancies, and reduce their concentration. Second, with fewer vacancies, positron diffusion lengths increase, allowing positrons to probe deeper into the film before annihilating. This dual effect enhances lateral grain alignment, leading to larger, better-aligned grains and improved lateral crystal quality. However, as indicated by the small diffraction peak at 34° in XRD, residual Mg metal begins to accumulate at these high flux rates, potentially leading to the formation of stacking faults.

The x-ray diffraction pole figures of the thin films, depicted in figure 4, reveal that stacking faults began to emerge when the Mg flux reached approximately 10.0 atoms·s^{-1}·nm^{-2}. This is evidenced by the appearance of the antiphase minor domain: $[\bar{1}\bar{1}2]_{Mg_2Sn} \parallel [10\bar{1}0]_{sapphire}$, coexisting with the major domain. Anti-phase minor domain spots, highlighted in yellow in figures 4(b)–(d), appear at directions 60° apart from the major domain spots. These stacking faults may exhibit increased occurrences at much higher flux

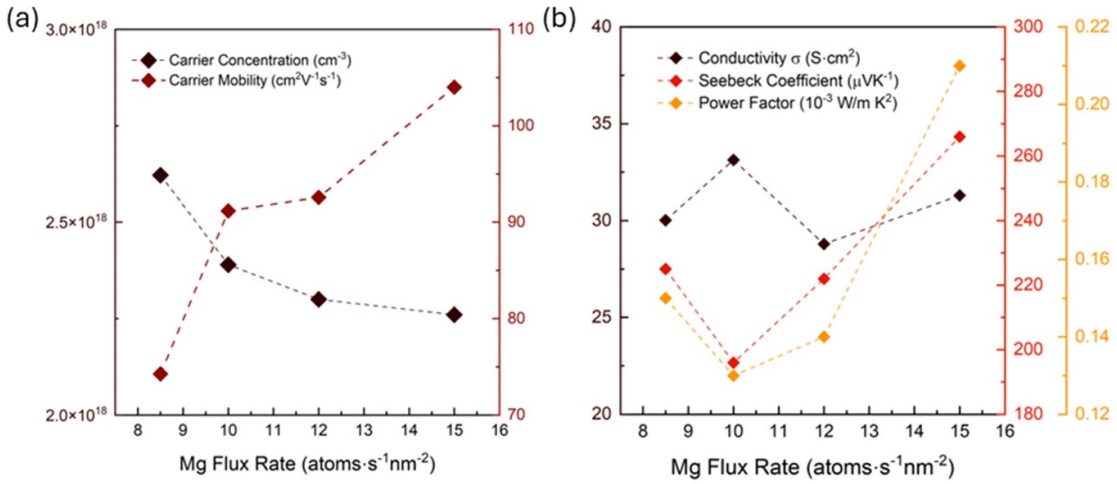

Figure 5. (a) Carrier concentration and mobility and (b) electrical conductivity, Seebeck coefficient and power factor as a function of Mg flux rate measured at RT.

rates, as also indicated by the PAS results showing a decrease in the S-parameter as a reference. While stacking faults are typically associated with reducing crystallinity due to their disruptive nature, they play a crucial role in managing strain within the crystal lattice in our Mg_2Sn (Ge) films with increasing Mg flux. Enhanced surface migration at higher Mg flux rates may promote larger horizontal grains, improving in-plane grain alignment and reducing the FWHM of the rocking curve. However, the same higher flux also introduces more vertical defects. Rapid incorporation of Mg atoms during vertical growth causes strain and disruptions, leading to non-ideal stacking sequences and promoting the formation of stacking faults. These conditions decrease vertical coherence length and increase the FWHM of the θ–2θ scan.

The RT Hall measurements of the films are plotted in figure 5(a). A slight decrease in carrier concentration with increasing Mg flux rate was observed. The decrease can be attributed to increasing grain boundary density. However, as we can observe, carrier mobility increased despite the decrease in carrier concentration, which is thanks to the enhancement of the crystallite quality and fewer large-scale defects formation at preferable higher Mg flux rates. The RT TE properties measurement in figure 5(b), shows that the electrical conductivity remains relatively stable which is because the decrease in carrier concentration was compensated for by an increase in carrier mobility. This maintains a stable product of p-type carrier concentration (p) and mobility (μ) thus keeping the conductivity constant. An initial decrease in the Seebeck coefficient was observed in the films grown at the Mg flux rates from 8 to 10 atoms·s^{-1}·nm^{-2}, followed by a consistent increase from 10 to 15 atoms·s^{-1}·nm^{-2}. This initial decrease of Seebeck coefficient from rates 8–10 atoms·s^{-1}·nm^{-2} might be related to the introduction of stacking faults which initially increase scattering, reducing the average energy of carriers and contributing to the Seebeck effect. However, in films grown at higher flux rates beyond 10 atoms·s^{-1}·nm^{-2}, the Seebeck coefficient increases, likely due to improved crystalline alignment, which reduces the scattering of higher-energy carriers. This suggests that at these higher flux rates, the beneficial influence of enhanced crystal order and a decrease in point defects outweigh the scattering introduced by the stacking faults. Moreover, the significant impact of the changes in the film properties by modulation of Mg flux rate can be clearly seen in the total thermal conductivity κ_{total} of the films shown in figure 6. As the Mg flux rate increased, we observed a decrease in the total thermal conductivity of the films which can be attributed to both the improved crystalline alignment of the films and the progressive modification of defect types. Initially, the films predominantly featured zero-dimensional point defects, such as vacancies, and one-dimensional like defects like dislocations. However, with higher Mg flux rates, the defects in the films were modified into two-dimensional planar defects which include stacking faults, which significantly contributed to enhanced phonon scattering and the resultant reduction in thermal conductivity.

4. Discussion

The results indicate that Mg_2Sn (Ge) films exhibit varying structural and TE properties based on the Mg flux rate during growth. The observed structural changes suggest that modulating the Mg flux during the growth of Mg_2Sn (Ge) films results in enhanced in-plane crystal alignment, nano-structural modifications associated with changes in lattice strain and grain boundaries, and the formation of higher dimensionality

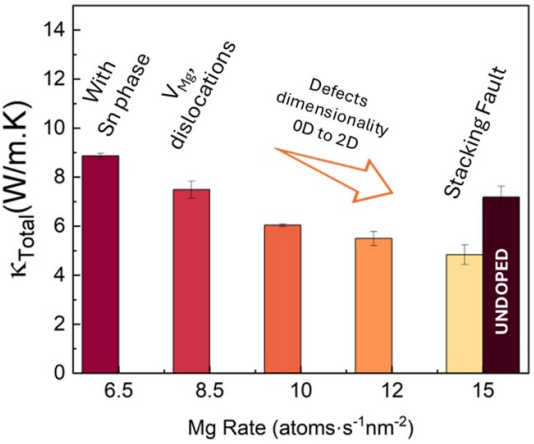

Figure 6. Total thermal conductivity at RT for Mg_2Sn (Ge) thin films.

defects, transitioning from vacancy-type and dislocation defects to dislocations, stacking faults and possible metastable phases. As stacking faults and grain boundaries become more prevalent, and the vacancy-type point defects are reduced, these results to an improvement of crystalline alignment and coherence and enhance carrier mobility. While stacking faults and grain boundaries typically scatter carriers and reduce mobility [47], in this study, the improved crystalline alignment and reduced vacancy defects may have mitigated their usual negative effects, resulting in the observed increase in mobility. This leads to more efficient carrier transport and higher average energy of carriers, resulting in a consistent increase in the Seebeck coefficient at higher Mg flux rates. Overall, we observe that higher Mg flux rates are required for the preferable TE properties of the films.

In general, the presence of these defects can reduce the electronic contribution to thermal conductivity κ_e by scattering charge carriers, but this effect is generally smaller compared to phonon scattering, thus, the alterations in the κ_{total} primarily stem from the decrease in lattice thermal conductivity κ_l contribution.

A similar behavior in the κ_l has been reported in GeTe-based TE materials wherein the evolution of defect structures from lower dimensionality defects to hierarchical domain structures via active control of Ge vacancies results to sharp decrease in thermal conductivity [48]. From the Debye-Callaway model, which accounts for phonon scattering by defects, the theoretical κ_l can be expressed as

$$\kappa_l = \frac{k_B}{2\pi^2 \nu}\left(\frac{k_B T}{\hbar}\right)^3 \int_0^{\theta_D/T} \frac{x^4 e^x}{\tau_C^{-1}(e^x-1)^2}\mathrm{d}x \tag{1}$$

where $x = \hbar\omega/k_B T$ is dimensionless, ω is the phonon frequency, $\hbar$ is the reduced Planck constant, ν is the average sound velocity, θ_D is the Debye temperature, and τ_C is the sum of the relaxation times of different phonon scattering mechanisms [49]. In the context of defect engineering, the pivotal factor lies in the manipulation of relaxation time τ_C, and defects are strategically introduced to amplify the phonon scattering by minimizing τ_C to reduce phonon mean free path. From here we see that the dimensionality of defects is a key parameter in understanding their impact on TE properties. If scattering processes can be analyzed separately, then the total relaxation time is:

$$\tau_C^{-1} = \sum_i \tau_i^{-1} = \tau_U^{-1} + \tau_N^{-1} + \tau_{PD}^{-1} + \tau_{DC}^{-1} + \tau_B^{-1} + \tau_{SF}^{-1} \ldots \tag{2}$$

where τ_i denotes the relaxation time corresponding to various phonon scattering mechanism, such as Umpklapp and normal phonon-phonon scattering (τ_U and τ_N), point defect scattering (τ_{PD}), dislocation core scattering (τ_{DC}), grain boundary scattering (τ_B), and stacking faults (τ_{ST}). Thus, the formation of higher dimensionality defects at higher Mg flux rates, such as stacking faults and increase in grain boundary density by the decrease in vertical grain size, can effectively lower κ_{total} of the films through additional phonon scattering provided by these defects.

5. Conclusions

Epitaxial Mg_2Sn (Ge) thin films were grown using MBE, with Mg flux rates varied from 8.5 to 15.0 atoms·s^{-1}·nm^{-2}, while maintaining a constant Sn (Ge) flux rate. The crystal properties and defect formation were investigated. Our study demonstrates that higher Mg flux rates improve lateral grain size and enhance in-plane crystal alignment. However, these higher flux rates also promote the formation of vertical defects, including stacking faults, which concurrently reduce and decrease vertical grain size and elevate microstrain within the lattice. The nuanced interplay between enhanced horizontal grain alignment and the introduction of higher-dimensionality defects resulted in a measurable decrease in thermal conductivity, an outcome that may favorably impact TE efficiency. Modulating Mg flux rates is demonstrated as an effective strategy for optimizing defect formation and enhancing the crystal quality of Mg-based thin films.

Data availability statement

All data that support the findings of this study are included within the article (and any supplementary files).

Acknowledgment

The research is funded by the JST Mirai Grant No. JPMJMI19A1. A part of this work was supported by 'Advanced Research Infrastructure for Materials and Nanotechnology in Japan (ARIM)' of the Ministry of Education, Culture, Sports, Science and Technology (MEXT) Proposal Number JPMXP1224NM5157. Thanks to Takanobu Hiroto for the assistance in obtaining the x-ray rocking curve measurements and x-ray pole figures, Noriyuki Okada for TEM sample preparation, and Makoto Oishi for TEM images acquisition. The first author expresses his sincerest gratitude to the Japanese Government for their financial support in carrying out this research through the Monbukagakusho (MEXT) Scholarship program.

ORCID iDs

Kenneth Magallon Senados https://orcid.org/0000-0002-1540-0862
Takashi Aizawa https://orcid.org/0000-0003-2357-5336
Takao Mori https://orcid.org/0000-0003-2682-1846

References

[1] Liu Z, Mao J, Liu T-H, Chen G and Ren Z 2018 Nano-microstructural control of phonon engineering for thermoelectric energy harvesting *MRS Bull.* **43** 181–6
[2] Shi X L, Zou J and Chen Z G 2020 Advanced thermoelectric design: from materials and structures to devices *Chem. Rev.* **120** 7399–515
[3] Shuai J, Sun Y, Tan X and Mori T 2020 Manipulating the Ge vacancies and Ge precipitates through Cr doping for realizing the high-performance GeTe thermoelectric material *Small* **16** 1906921
[4] Zhao C, Li Z, Fan T, Xiao C and Xie Y 2020 Defects engineering with multiple dimensions in thermoelectric materials *Research* **2020** 9652749
[5] Zheng Y, Slade T J, Hu L, Tan X Y, Luo Y, Luo Z Z, Xu J, Yan Q and Kanatzidis M G 2021 Defect engineering in thermoelectric materials: what have we learned? *Chem. Soc. Rev.* **50** 9022–54
[6] Liu Z *et al* 2021 Demonstration of ultrahigh thermoelectric efficiency of ∼7.3% in Mg_3Sb_2/MgAgSb module for low-temperature energy harvesting *Joule* **5** 1196–208
[7] Tomeda A, Ishibe T, Taniguchi T, Okuhata R, Watanabe K and Nakamura Y 2018 Enhanced thermoelectric performance of Ga-doped ZnO film by controlling crystal quality for transparent thermoelectric films *Thin Solid Films* **666** 185–90
[8] Ohtsuki T and Higashiwaki M 2023 Crystallinity degradation and defect development in $(Al_xGa_{1-x})_2O_3$ thin films with increased Al composition *J. Vac. Sci. Technol.* A **41** 042712
[9] Wang B, Wong K Y, Yang S and Chen T 2016 Crystallinity and defect state engineering in organo-lead halide perovskite for high-efficiency solar cells *J. Mater. Chem.* A **4** 3806–12
[10] Biswas K, Ren Z, Grin Y, Lee K H, Mori T and Chen L 2022 Thermoelectric materials science and technology toward applications *Appl. Phys. Lett.* **121** 070401
[11] Nandihalli N, Liu C-J and Mori T 2020 Polymer based thermoelectric nanocomposite materials and devices: fabrication and characteristics *Nano Energy* **78** 105186
[12] Haras M and Skotnicki T 2018 Thermoelectricity for IoT—a review *Nano Energy* **54** 461–76
[13] George A, Yanagisawa R, Anufriev R, He J, Yoshie N, Tsujii N, Guo Q, Mori T, Volz S and Nomura M 2019 Thermoelectric enhancement of silicon membranes by ultrathin amorphous films *ACS Appl. Mater. Interfaces* **11** 12027–31
[14] Narayan J and Larson B C 2003 Domain epitaxy: a unified paradigm for thin film growth *J. Appl. Phys.* **93** 278–85
[15] Wandelt K 2013 *Surface and Interface Science* (Wiley)
[16] Chambers S A 2000 Epitaxial growth and properties of thin film oxides *Surf. Sci. Rep.* **39** 105–80
[17] Evans J W, Thiel P A and Bartelt M C 2006 Morphological evolution during epitaxial thin film growth: formation of 2D islands and 3D mounds *Surf. Sci. Rep.* **61** 1–128
[18] Lüth H 2015 *Solid Surfaces, Interfaces and Thin Films* (Springer International Publishing)

[19] He Z, Yang M, Wang Z, Chen H, Zhang X, Jiang Q, Murugadoss V, Huang M, Guo Z and Zhang H 2022 Optimization of segmented thermoelectric devices composed of high-temperature thermoelectric material La_2Te_3 *Adv. Compos. Hybrid Mater.* **5** 2884–95
[20] Kaiser N 2002 Review of the fundamentals of thin-film growth *Appl. Opt.* **41** 3053
[21] Burcea R *et al* 2022 Influence of generated defects by Ar implantation on the thermoelectric properties of ScN *ACS Appl. Energy Mater.* **5** 11025–33
[22] Seo D K, Kim J H, Kim J H and Cho H K 2012 Remarkable increase of thermoelectric power factor using plasma treatment in layered $InGaO_3$ $(ZnO)_m$ thin films *Surf. Interface Anal.* **44** 1519–21
[23] Ho C Y, Wang Y, Liu C P and Yu K M 2022 Controlling electrical and optical properties of wurtzite $Cd_xZn_{1-x}O$ with high Cd contents via native defects manipulation by low-temperature annealing *J. Appl. Phys.* **131** 205102
[24] Dhanaraj G, Byrappa K, Prasad V and Dudley M 2010 *Springer Handbook of Crystal Growth* (Springer)
[25] Anon 2015 *Handbook of Crystal Growth* (Elsevier)
[26] Aizawa T, Ohkubo I, Lima M S L, Sakurai T and Mori T 2019 Fabrication of $Mg_2Sn(111)$ film by molecular beam epitaxy *J. Vac. Sci. Technol.* A **37** 061513
[27] Lima M S L, Aizawa T, Ohkubo I, Sakurai T and Mori T 2021 Improvement of power factor in the room temperature range of $Mg_2Sn_{1-x}Ge_x$ *Jpn. J. Appl. Phys.* **60** SBBF06
[28] Lima M S L, Aizawa T, Ohkubo I, Baba T, Sakurai T and Mori T 2021 High power factor in epitaxial Mg_2Sn thin films via Ga doping *Appl. Phys. Lett.* **119** 254101
[29] Ohkubo I, Murata M, Ohi A, Lima M S L, Sakurai T, Aizawa T and Mori T 2023 Structural effects on the performance of microfabricated in-plane $\boldsymbol{\pi}$ -type thermoelectric devices composed of p-type $Mg_2Sn_{0.8}Ge_{0.2}$ and n-type Bi layers *Appl. Phys. Lett.* **122** 243901
[30] Ohkubo I, Murata M, Lima M S L, Sakurai T, Sugai Y, Ohi A, Aizawa T and Mori T 2022 Miniaturized in-plane π-type thermoelectric device composed of a II–IV semiconductor thin film prepared by microfabrication *Mater. Today Energy* **28** 101075
[31] Ohkubo I, Aizawa T, Senados K M, Lima M S L, Sakurai T and Mori T 2023 Surface chemical states and structures of epitaxial Mg_2Sn thermoelectric thin films *Jpn. J. Appl. Phys.* **62** 108004
[32] Senados K M, Lima M S L, Aizawa T, Ohkubo I, Baba T, Uedono A, Sakurai T and Mori T 2024 Influence of Ge to the formation of defects in epitaxial $Mg_2Sn_{1-x}Ge_x$ thermoelectric thin films *Jpn. J. Appl. Phys.* **63** 02SP40
[33] Ohkubo I, Aizawa T, Nakamura K and Mori T 2021 Control of competing thermodynamics and kinetics in vapor phase thin-film growth of nitrides and borides *Front. Chem.* **9** 642388
[34] Baba T, Taketoshi N and Yagi T 2011 Development of ultrafast laser flash methods for measuring thermophysical properties of thin films and boundary thermal resistances *Jpn. J. Appl. Phys.* **50** 11RA01
[35] Kakefuda Y, Yubuta K, Shishido T, Yoshikawa A, Okada S, Ogino H, Kawamoto N, Baba T and Mori T 2017 Thermal conductivity of $PrRh_{4.8}B_2$, a layered boride compound *APL Mater.* **5** 126103
[36] Gao W, Liu Z, Baba T, Guo Q, Tang D-M, Kawamoto N, Bauer E, Tsujii N and Mori T 2020 Significant off-stoichiometry effect leading to the N-type conduction and ferromagnetic properties in titanium doped Fe_2VAl thin films *Acta Mater.* **200** 848–56
[37] Baba T, Baba T, Ishikawa K and Mori T 2021 Determination of thermal diffusivity of thin films by applying Fourier expansion analysis to thermo-reflectance signal after periodic pulse heating *J. Appl. Phys.* **130** 225107
[38] Gerstein B C, Chung P L and Danielson G C 1966 Thermal study of group II–IV semiconductors—I. Heat capacity of Mg_2Ge in the range 5–300°K *J. Phys. Chem. Solids* **27** 1161–5
[39] Uedono A, Ishibashi S, Tenjinbayashi K, Tsutsui T, Nakahara K, Takamizu D and Chichibu S F 2012 Defect characterization in Mg-doped GaN studied using a monoenergetic positron beam *J. Appl. Phys.* **111** 014508
[40] Uedono A, Ueno W, Yamada T, Hosoi T, Egger W, Koschine T, Hugenschmidt C, Dickmann M and Watanabe H 2020 Voids and vacancy-type defects in SiO_2/GaN structures probed by monoenergetic positron beams *J. Appl. Phys.* **127** 054503
[41] Uedono A, Ishibashi S, Oshima N and Suzuki R 2013 Positron annihilation spectroscopy on nitride-based semiconductors *Jpn. J. Appl. Phys.* **52** 08JJ02
[42] Tuomisto F and Makkonen I 2013 Defect identification in semiconductors with positron annihilation: experiment and theory *Rev. Mod. Phys.* **85** 1583–631
[43] Ohkubo I, Christen H M, Kalinin S V, Jellison G E, Rouleau C M and Lowndes D H 2004 High-throughput growth temperature optimization of ferroelectric $Sr_xBa_{1-x}Nb_2O_6$ epitaxial thin films using a temperature gradient method *Appl. Phys. Lett.* **84** 1350–2
[44] Saito W, Hayashi K, Huang Z, Dong J, Li J-F and Miyazaki Y 2020 Enhancing the thermoelectric performance of Mg_2Sn single crystals via point defect engineering and Sb doping *ACS Appl. Mater. Interfaces* **12** 57888–97
[45] Saito W, Hayashi K, Dong J, Li J-F and Miyazaki Y 2020 Control of the thermoelectric properties of Mg_2Sn single crystals via point-defect engineering *Sci. Rep.* **10** 2020
[46] Saito W *et al* 2021 Chemical-pressure-induced point defects enable low thermal conductivity for Mg_2Sn and Mg_2Si single crystals *ACS Appl. Energy Mater.* **4** 5123–31
[47] Quirk J, Rothmann M, Li W, Abou-Ras D and McKenna K P 2024 Grain boundaries in polycrystalline materials for energy applications: first principles modeling and electron microscopy *Appl. Phys. Rev.* **11** 011308
[48] Jiang Y *et al* 2022 Evolution of defect structures leading to high ZT in GeTe-based thermoelectric materials *Nat. Commun.* **13** 6087
[49] Callaway J and von Baeyer H C 1960 Effect of point imperfections on lattice thermal conductivity *Phys. Rev.* **120** 1149–54